electronic reprint

Journal of
Applied Crystallography
ISSN 0021-8898

Deconvolution of the instrumental functions in powder X-ray diffractometry

T. Ida and H. Toraya

Journal of
Applied Crystallography
ISSN 0021-8898

Received 30 August 2001
Accepted 7 November 2001

Deconvolution of the instrumental functions in powder X-ray diffractometry

T. Ida* and H. Toraya

Ceramics Research Laboratory, Nagoya Institute of Technology, Asahigaoka, Tajimi, Gifu 507-0071, Japan. Correspondence e-mail: ida@crl.nitech.ac.jp

A novel method to deconvolute the instrumental aberration functions from the experimental powder X-ray data has been developed. The method is based on the combination of scale transformation, interpolation of data and fast Fourier transformation. The effects of axial divergence, flat specimen, sample transparency and spectroscopic profile of the source X-ray are eliminated from the entire observed diffraction pattern in three-step operations. The errors in the deconvoluted data propagated from the statistical uncertainty in the source data are approximated by the reciprocal of the square root of the correlation between the reciprocal of the variance in the source data and the squared instrumental function. The deconvolution of the instrumental aberration functions enables automatic correction of peak shift and line broadening, and supplies narrow and symmetric peak profiles for a well crystallized sample, which can be fitted by a simple model function. It will be useful in preparatory data processing for precise line profile analysis, accurate determination of lattice parameters and whole pattern fitting for crystal structure analysis.

1. Introduction

It has been well recognized that experimental X-ray diffraction profiles are convolutions of the incident X-ray spectral distribution, the various instrumental aberrations and the intrinsic diffraction pattern of the powder or polycrystalline sample (Ladell *et al.*, 1959). A variety of methods have been proposed for the elimination of instrumental broadening, including that caused by the α_1–α_2 doublet (Rachinger, 1948; Stokes, 1948; Keating, 1959; Gangulee, 1970; Ladell *et al.*, 1975). However, none of these methods can be used to eliminate the instrumental aberrations from the entire observed diffraction pattern in a one-step operation, except Keating's method for elimination of the α_2 peak, which is based on a kind of series expansion. The other methods restricted the solution of this problem to a small part of the pattern (a single diffraction line). It is impossible to deconvolute all of the instrumental effects from an entire diffraction pattern by a standard Fourier method, because the profile of the instrumental function for powder diffractometry is varied in a complex manner depending on the diffraction angle 2θ. It seems that no significant improvement has been achieved in Fourier-based methods for elimination of instrumental aberration from experimental peak profiles, after the pioneering work of Stokes (1948).

Recently, we have elucidated concrete mathematical formulae for the instrumental aberration functions of widely utilized powder diffractometers with Bragg–Brentano geometry, and that the experimental diffraction peak profiles are well reproduced with the model profile function synthesized by multiple convolutions of a symmetric function with those instrumental functions (Ida, 1998*a*,*b*; Ida & Kimura, 1999*a*,*b*). As the accurate mathematical formula of the instrumental function is known, the intrinsic diffraction profiles of the sample should be extracted from the experimental profiles by the deconvolution based on Fourier methods.

In this paper, we present a novel method for eliminating the aberrations caused by the effects of axial divergence, flat specimen, sample transparency and α_1–α_2 doublet of the source X-ray. The method is based on the combination of scale transformation, interpolation of data and fast Fourier transformation. The effects of instrumental aberrations can be removed from the entire diffraction pattern in a three-step operation. We also discuss how the statistical errors in source data are propagated through the deconvolution process, and propose an approximate indicator of the error in the deconvoluted data, which enables subsequent application of a weighted least-squares method to analyse the deconvoluted data.

2. Theoretical framework

Although the profile of the total instrumental function for powder diffractometry varies in a complex manner depending on the diffraction angle 2θ, each component of the synthesized instrumental function is not formidably complicated, as has been shown in previous reports on this subject (Cheary & Coelho, 1992, 1998; Ida, 1998*a*; Ida & Kimura, 1999*a*,*b*). The dependence of component instrumental profile on the diffraction angle can be removed by application of appro-

priate scale transformation to the variable, as shown in the following sections.

2.1. Scale transformation

In this section, a general method to treat the instrumental function, the profile of which varies depending on the diffraction angle 2θ, is described. We assume that the source diffraction pattern is represented by the scattering intensity data $\{S_m\}$ for the diffraction angle $\{2\theta_m\}$ ($m = 0, \ldots, M-1$), where M is the number of data points.

Provided that the change in the profile of the instrumental function is specified only by a line-width parameter $\gamma(2\theta)$ dependent on 2θ, the instrumental function $\omega(\Delta 2\theta)$ can be written as

$$\omega(\Delta 2\theta; 2\theta) = [1/\beta\gamma(2\theta)]w[\Delta 2\theta/\beta\gamma(2\theta)], \quad (1)$$

where β is an arbitrary constant independent of 2θ.

We define a function $G(x)$ by

$$G(2\theta) \equiv \int [\mathrm{d}(2\theta)/\gamma(2\theta)], \quad (2)$$

and change the abscissa from 2θ to χ, by the equation $\chi = G(2\theta)$. Then, the following relation is derived,

$$\Delta\chi/\Delta 2\theta = 1/\gamma(2\theta), \quad (3)$$

which means that the small width $\gamma(2\theta)$ on the 2θ scale corresponds to a constant step in χ scale. By multiplying the scattering data by $\gamma(2\theta)$, the local integrated intensity is maintained; that is, the diagram becomes equivalent to that convoluted with the constant instrumental function: $\beta^{-1}w(\chi/\beta)$, on the transformed scale.

Here we take the angular velocity, polarization and powder diffraction intensity factors given by (Lipson & Langford, 1999)

$$C(2\theta) = (1 + A\cos^2 2\theta)/(1 + A)\sin\theta\sin 2\theta \quad (4)$$

and

$$A = \cos 2\theta_M, \quad (5)$$

where $2\theta_M$ is the diffraction angle of the monochromator, to correct the scattering intensity. The overall scale transform from the source data, $\{2\theta_m\}$ and $\{S_m\}$, given by

$$\chi_m \longleftarrow G(2\theta_m), \quad (6)$$

and

$$\eta_m \longleftarrow S_m\gamma(2\theta_m)/C(2\theta_m), \quad (7)$$

is applied before the following deconvolution process.

When the source data are collected by a counting method, the intensity data are accompanied with the errors given by $\Delta S_m = S_m^{1/2}$. As a result of propagation of the error, the source error $\{\Delta S_m\}$ is considered to be changed to $\{s_m\}$ as follows,

$$s_m \longleftarrow \Delta S_m\gamma(2\theta_m)/C(2\theta_m). \quad (8)$$

2.2. Interpolation of data

The scale-transformed abscissa $\{\chi_m\}$, ordinate $\{\eta_m\}$ and error $\{s_m\}$ ($m = 0, \ldots, M-1$) data are not sampled at evenly spaced intervals. In order to utilize fast Fourier transform, they are interpolated to create evenly spaced data, the total number of which should be an integer power of 2.

A correction should be applied to the error data $\{s_m\}$, because the sampling intervals are changed by interpolation. When the local density of the data points is changed from n to n' by interpolation, the statistical properties of the data are maintained by changing the error data from σ to $(n'/n)^{1/2}\sigma$. Therefore, the error data $\{s_m\}$ are further modified to $\{s'_m\}$ by the following equation,

$$s'_m \longleftarrow \left[(2\theta_{M-1} - 2\theta_0)N\gamma(2\theta_m)/(\chi_{M-1} - \chi_0)M\right]^{1/2} s_m, \quad (9)$$

before the interpolation process.

Then, evenly spaced abscissa $\{x_n\}$, ordinate $\{y_n\}$, and error $\{\sigma_n\}$ ($n = 0, \ldots, N-1$) data are created from the source data $\{\chi_m\}$, $\{\eta_m\}$, $\{s'_m\}$ ($m = 0, \ldots, M-1$), by a cubic spline interpolation (Press *et al.*, 1986).

2.3. Deconvolution of instrumental function

The Fourier transform $W(\xi)$ of the instrumental function $w(x)$ is given by

$$W(\xi) = \int_{-\infty}^{\infty} w(x)\exp(2\pi i\xi x)\,\mathrm{d}x. \quad (10)$$

Assuming that the instrumental function is expressed by a discrete form $\{w_n\}$ ($n = 0, \ldots, N-1$), the discrete Fourier transform is formally given by

$$W_k = \sum_{n=0}^{N-1} w_n \exp(2\pi ikn/N) \quad (k = -N/2, \ldots, N/2), \quad (11)$$

where the periodicity $W_{-k} = W_{N-k}$ is implicitly assumed.

The Fourier transform $W(\xi)$ of the instrumental function $w(x)$ and the discrete Fourier coefficients W_k satisfy the following relation,

$$W_k = W(k/N\Delta) \quad (k = -N/2, \ldots, N/2), \quad (12)$$

where Δ is the sampling interval of the data $\{y_n\}$. Since an instrumental function may have singularities, equation (12) is easier to handle than equation (11) in numerical calculations, when the analytical formula of the Fourier transform is available.

The deconvoluted intensity data $\{z_n\}$ from the source data $\{y_n\}$ are calculated by the inverse Fourier transform

$$z_n = (1/N)\sum_{k=0}^{N-1}(Y_k/W_k)\exp(-2\pi ikn/N), \quad (13)$$

where $\{Y_k\}$ is the discrete Fourier transform of $\{y_n\}$.

2.4. Propagation of errors through deconvolution

In this section, we discuss how the statistical errors $\{\sigma_n\}$ attached to the source data $\{y_n\}$ are propagated into the deconvoluted data $\{z_n\}$ through the deconvolution process.

The convolution is generally expressed by

$$y_n = \sum_{m=0}^{N-1} z_{n-m} w_m, \tag{14}$$

where $\{w_n\}$ is the discrete form of the instrumental function. We can define the inverse instrumental function $\{w_n^{(-1)}\}$ by

$$w_n^{(-1)} \equiv (1/N) \sum_{k=0}^{N-1} (1/W_k) \exp(-2\pi ikn/N), \tag{15}$$

where $\{W_k\}$ is the discrete Fourier transform of the instrumental function. Then, $\{z_n\}$ is the convolution of $\{y_n\}$ and $\{w_n^{(-1)}\}$; that is,

$$z_n = \sum_{m=0}^{N-1} y_{n-m} w_m^{(-1)}. \tag{16}$$

The element of the covariance matrix S_{mn} ($m, n = 0, \ldots, N-1$) for the deconvoluted data $\{z_n\}$ is immediately given by

$$\begin{aligned} S_{mn} &= \big\langle (z_m - \langle z_m \rangle)(z_n - \langle z_n \rangle) \big\rangle \\ &= \sum_{l=0}^{N-1} \sigma_l^2 w_{m-l}^{(-1)} w_{n-l}^{(-1)}, \end{aligned} \tag{17}$$

where $\langle z \rangle$ means the average of the variable z (see Appendix *A*1). The above equation shows that the off-diagonal elements of the covariance matrix (S_{mn}) are generally not equal to zero. In principle, this problem can be exactly treated as follows.

In case that the off-diagonal elements have non-zero values, the weighted least-squares fitting method is identical to the problem of minimization of the quantity

$$\chi^2 = \sum_{m=0}^{N-1} \sum_{n=0}^{N-1} [z_m - f(x_m)] T_{mn} [z_n - f(x_n)], \tag{18}$$

where $f(x)$ is the model function, and T_{mn} is the element of the inverse covariance matrix (weight matrix). The weight-matrix element T_{mn} is related to the source error $\{\sigma_n\}$ by the equation (see Appendix *A*2)

$$T_{mn} = \sum_{k=0}^{N-1} \sigma_k^{-2} w_{k-m} w_{k-n}. \tag{19}$$

By applying (18) and (19), one can achieve a proper estimation of fitting parameters.

However, usual library programs for least-squares fitting cannot deal with the weight matrix with non-zero off-diagonal elements. Furthermore, huge memory space and efforts for calculation will be needed if all the elements of the weight matrix are explicitly taken into account in the case of a large number of data points.

A usual fitting program can still be applied, on the assumption that the diagonal elements of the weight matrix or the covariance matrix are the indicators of the error in the deconvoluted data.

When we define the diagonal elements of the weight and covariance matrices as δ_n^{-2} and ε_n^2, respectively, they are related to the error in the source data by

$$\delta_n^{-2} \equiv T_{nn} = \sum_{l=0}^{N-1} \sigma_l^{-2} w_{l-n}^2 \tag{20}$$

and

$$\varepsilon_n^2 \equiv S_{nn} = \sum_{l=0}^{N-1} \sigma_l^2 \Big[w_{n-l}^{(-1)} \Big]^2, \tag{21}$$

which mean that $\{\delta_n^{-2}\}$ is the correlation of the reciprocal variance $\{\sigma_n^{-2}\}$ with the squared instrumental function $\{w_n^2\}$, and that $\{\varepsilon_n^2\}$ is the convolution of the variance $\{\sigma_n^2\}$ with the squared inverse instrumental function $\{(w_n^{(-1)})^2\}$.

By applying the discrete correlation and convolution theorems, the following convenient formulae are derived,

$$\delta_n^{-2} = \frac{1}{N} \sum_{k=0}^{N-1} V_k^{(-1)} \Big[W_k^{(2)} \Big]^* \exp(-2\pi ikn/N), \tag{22}$$

and

$$\varepsilon_n^2 = \frac{1}{N} \sum_{k=0}^{N-1} V_k W_k^{(-2)} \exp(-2\pi ikn/N), \tag{23}$$

where $\{V_k\}$, $\{V_k^{(-1)}\}$ and $\{W_k^{(-2)}\}$ are the Fourier transforms of the variance $\{\sigma_n^2\}$, reciprocal variance $\{\sigma_n^{-2}\}$ and the squared inverse instrumental function $\{(w_n^{(-1)})^2\}$, respectively, and $[W_k^{(2)}]^*$ is the complex conjugate of the Fourier transform of the squared instrumental function $\{w_n^2\}$.

The two indicators of the error in the deconvoluted data, $\{\delta_n\}$ and $\{\varepsilon_n\}$, do not necessarily coincide. The difference between the two error indicators will be discussed later.

2.5. Smoothing data

The deconvolution of the instrumental function from the experimental data always exaggerates the noise in the source data. Application of a slight smoothing filter is effective to suppress the unwanted increase of the noisy structure. The Gaussian filtering is implemented by the convolution with the function

$$w_G(x; \gamma_G) = (1/\pi^{1/2}\gamma_G) \exp(-x^2/\gamma_G^2), \tag{24}$$

the analytical Fourier transform of which is given by

$$W_G(\xi) = \int_{-\infty}^{\infty} w_G(x) \exp(2\pi i\xi x)\, \mathrm{d}x = \exp(-\pi^2 \xi^2 \gamma_G^2). \tag{25}$$

The minimal width of the Gaussian filter γ_G to suppress the increase of the noise on deconvolution is determined by

$$\big|(W_G)_{N/2}\big| = \big|(W_O)_{N/2}\big|, \tag{26}$$

where $\{(W_O)\}$ is the Fourier transform of the target instrumental function, or more concretely,

$$\gamma_G^2 = -\ln \big|(W_O)_{N/2}\big|^2 / 2\pi^2 \xi_{N/2}^2, \tag{27}$$

where

$$\xi_{N/2} = 1/2\Delta, \tag{28}$$

in which Δ is the sampling interval and $\xi_{N/2}$ is equivalent to the Nyquist critical frequency in time series analysis.

This smoothing process has a slight broadening effect, the width of which is comparable with the sampling interval of the interpolated data, and narrower than the measurement step. Even if a precise profile analysis is required after the deconvolution, this broadening effect can easily be taken into

account as a convolution with the Gaussian function with the known width.

3. Instrumental functions

3.1. Axial divergence effect

The instrumental function for the axial divergence aberration is given by

$$\omega_A(\Delta 2\theta; 2\theta) = (2/\pi\psi^2)\exp[(t - 1/t)(\Delta 2\theta/\psi^2)] \times K_0[(t + 1/t)(|\Delta 2\theta|/\psi^2)], \quad (29)$$

where $t \equiv \tan\theta$, $\Psi \equiv 2(\ln 2)^{1/2}\psi$ is the full width at half-maximum (FWHM) of the axial divergence, and $K_0(x)$ is the modified Bessel function of the second kind (Ida, 1998*a*). The profile of this function varies on the diffraction angle, in a complex manner as shown in Fig. 1(*a*), and cannot satisfy the requirement given in equation (1); that is, the profile of the function $\omega_A(\Delta 2\theta; 2\theta)$ cannot be determined by a single line-width parameter.

However, this function is, fortunately, exactly equivalent to the convolution of the following two functions:

$$\omega_{A-}(\Delta 2\theta) = \begin{cases} (2t/\pi^{1/2}\psi^2)(-\psi^2/2t\Delta 2\theta)^{1/2}\exp(2t\Delta 2\theta/\psi^2) \\ \quad \text{for } \Delta 2\theta \le 0 \\ 0 \quad \text{elsewhere} \end{cases} \quad (30)$$

and

$$\omega_{A+}(\Delta 2\theta) = \begin{cases} (2/\pi^{1/2}t\psi^2)(t\psi^2/2\Delta 2\theta)^{1/2}\exp(-2\Delta 2\theta/t\psi^2) \\ \quad \text{for } \Delta 2\theta \ge 0 \\ 0 \quad \text{elsewhere} \end{cases} \quad (31)$$

That is,

$$\omega_A(\Delta 2\theta) = \omega_{A-}(\Delta 2\theta) * \omega_{A+}(\Delta 2\theta) = \int_{-\infty}^{\infty} \omega_{A-}(\Delta 2\theta - y)\omega_{A+}(y)\,dy. \quad (32)$$

Figs. 1(*b*) and 1(*c*) show how the function $\omega_A(\Delta 2\theta)$ is decomposed to the two component functions $\omega_{A-}(\Delta 2\theta)$ and $\omega_{A+}(\Delta 2\theta)$.

By applying the scale transform given by the equations

$$\Delta 2\theta/\Delta x = \gamma_1(2\theta) = 2/\tan\theta \quad (33)$$

and

$$x = G_1(2\theta) = -\ln(\cos\theta) \quad (34)$$

to the lower-angle component function $\omega_{A-}(\Delta 2\theta)$, we obtain a formula of the instrumental function independent of the diffraction angle:

$$w_{A-}(x) = \begin{cases} \exp(x/\beta_A)/\beta_A(-\pi x/\beta_A)^{1/2} & \text{for } x \le 0 \\ 0 & \text{elsewhere} \end{cases} \quad (35)$$

where

$$\beta_A = \psi^2/4. \quad (36)$$

The analytical formula of the Fourier transform of $w_{A-}(x)$ is given by

$$W_{A-}(\xi) = \int_{-\infty}^{\infty} w_{A-}(x)\exp(2\pi i\xi x)\,dx = \left\{\left[\left(4\pi^2\xi^2\beta_A^2 + 1\right)^{1/2} + 1\right]^{1/2} - i\left[\left(4\pi^2\xi^2\beta_A^2 + 1\right)^{1/2} - 1\right]^{1/2}\right\}\left[2\left(4\pi^2\xi^2\beta_A^2 + 1\right)\right]^{-1/2}. \quad (37)$$

Fig. 2 shows the axial divergence and its component functions plotted on the $-\ln(\cos\theta)$ scale. It is found that the function $\omega_{A-}(\Delta 2\theta)$ keeps the same profile on the current scale.

For the higher-angle component function $\omega_{A+}(\Delta 2\theta)$, application of the scale transform

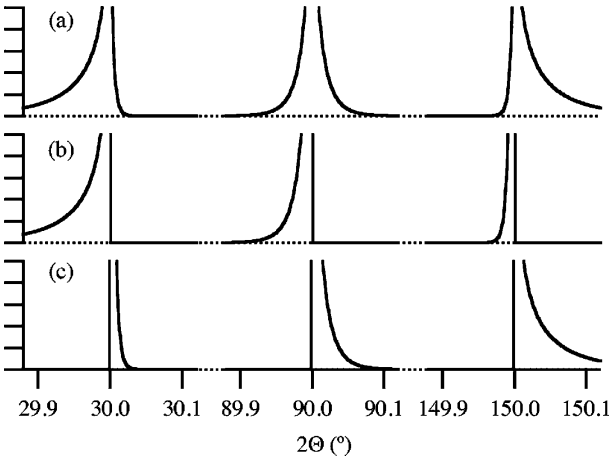

Figure 1
The dependence of the axial divergence aberration functions on the diffraction angle. (*a*) The axial divergence aberration function $\omega_A(\Delta 2\theta)$, (*b*) the lower-angle component $\omega_{A-}(\Delta 2\theta)$, and (*c*) the higher-angle component $\omega_{A+}(\Delta 2\theta)$ for the axial divergence angle $\Phi_A = 5°$.

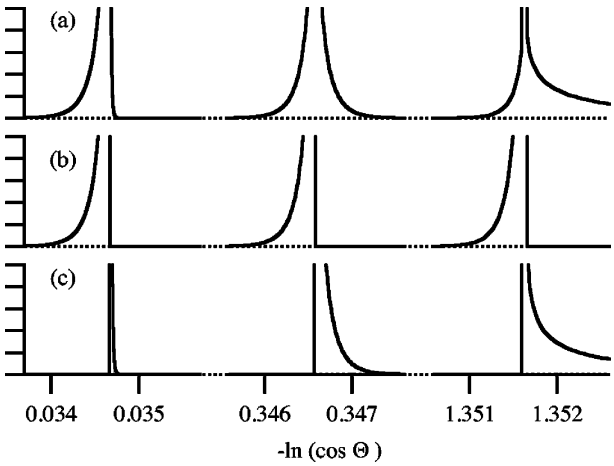

Figure 2
The effect of the scale transform $-\ln(\cos\theta)$ on the axial divergence aberration functions shown in Fig. 1.

$$\Delta 2\theta/\Delta x = \gamma_2(2\theta) = 2\tan\theta, \tag{38}$$

with

$$x = G_2(2\theta) = \ln(\sin\theta), \tag{39}$$

gives the angle-independent formula

$$w_{A+}(x) = \begin{cases} \exp(-x/\beta_A)/\beta_A(\pi x/\beta_A)^{1/2} & \text{for } x \geq 0 \\ 0 & \text{elsewhere} \end{cases} \tag{40}$$

and the Fourier transform is given by

$$\begin{aligned} W_{A+}(\xi) &= \int_{-\infty}^{\infty} w_{A+}(x)\exp(2\pi i\xi x)\,\mathrm{d}x \\ &= \left\{\left[\left(4\pi^2\xi^2\beta_A^2+1\right)^{1/2}+1\right]^{1/2} + i\left[\left(4\pi^2\xi^2\beta_A^2+1\right)^{1/2} - 1\right]^{1/2}\right\}\left[2\left(4\pi^2\xi^2\beta_A^2+1\right)\right]^{-1/2}. \end{aligned} \tag{41}$$

Fig. 3 shows the axial divergence and its component functions plotted on the $\ln(\sin\theta)$ scale. The higher-angle component function $\omega_{A+}(\Delta\theta)$ is found to keep the same profile on this scale.

Since equations (30) and (31) have an identical structure to equation (1), the axial divergence effect can be eliminated for the entire diffraction pattern by two step deconvolutions of $\omega_{A-}(\Delta 2\theta)$ and $\omega_{A+}(\Delta 2\theta)$.

3.2. Flat-specimen effect

The flat-specimen aberration function on the 2θ scale is given by (Ida & Kimura, 1999*a*)

$$\omega_F(\Delta 2\theta) = \begin{cases} (1/2\beta_F\gamma_1)(-\Delta 2\theta/\beta_F\gamma_1)^{-1/2} \\ \quad \text{for } -\beta_F\gamma_1 < \Delta 2\theta < 0, \\ 0 \quad \text{elsewhere} \end{cases} \tag{42}$$

where we define $\beta_F \equiv \Phi_F^2/4$ for the equatorial divergence angle Φ_F. The definition of γ_1 is given in equation (33). The dependence of the profile of $\omega_F(\Delta 2\theta)$ is shown in Fig. 4(*a*).

By applying the scale transform $G_1(2\theta) = -\ln(\cos\theta)$, the angle-independent instrumental function is derived as

$$w_F(x) = \begin{cases} (1/2\beta_F)(-x/\beta_F)^{-1/2} \\ \quad \text{for } -\beta_F < x < 0 \\ 0 \quad \text{elsewhere} \end{cases} \tag{43}$$

The profile of the instrumental function on the transformed scale is shown in Fig. 4(*b*).

The Fourier transform of the instrumental function is given by

$$\begin{aligned} W_F(\xi) &= \int_{-\infty}^{\infty} w_F(x)\exp(2\pi i\xi x)\,\mathrm{d}x \\ &= [1/2(\xi\beta_F)^{1/2}]\{C[2(\xi\beta_F)^{1/2}] - iS[2(\xi\beta_F)^{1/2}]\}, \end{aligned} \tag{44}$$

where $C(x)$ and $S(x)$ are the Fresnel functions defined by

$$S(x) \equiv \int_0^x \sin(\pi t^2/2)\,\mathrm{d}t \tag{45}$$

and

$$C(x) \equiv \int_0^x \cos(\pi t^2/2)\,\mathrm{d}t. \tag{46}$$

Reliable computer routines to evaluate the Fresnel functions are available (Press *et al.*, 1986).

3.3. Sample transparency effect

If the sample has such high transparency that the penetration depth of the source X-ray is comparable with or longer than the thickness of the sample, the angular dependence of the transparency effect becomes complicated (Ida & Kimura, 1999*b*). In such cases, it may be better to conduct an analysis applying the model profile function with convoluted formula, rather than deconvolution based on Fourier methods.

When the penetration depth is sufficiently shorter than the thickness of the sample, the deconvolution can be easily achieved. In this case, the instrumental function on the 2θ scale is given by

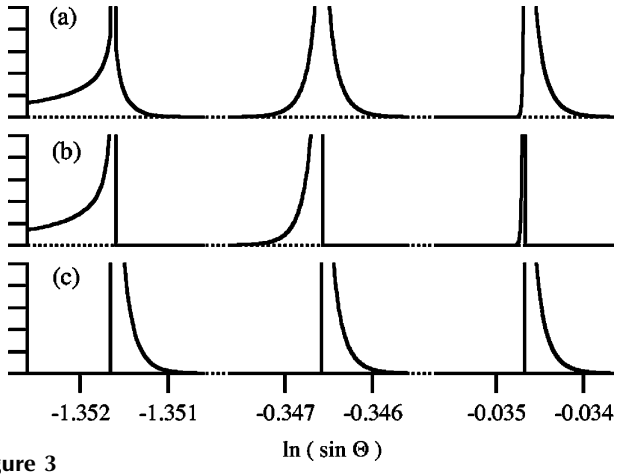

Figure 3
The effect of the scale transform $\ln(\sin\theta)$ on the axial divergence aberration functions shown in Fig. 1.

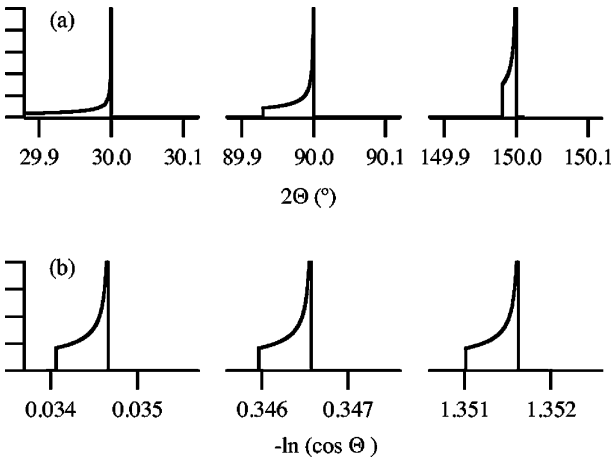

Figure 4
The dependence of the flat-specimen aberration function on the diffraction angle. (*a*) The instrumental function $\omega_F(\Delta 2\theta)$ for the equatorial divergence angle of $\Phi_F = 2^\circ$ on the 2θ scale, and (*b*) that plotted on the $-\ln(\cos\theta)$ scale.

$$\omega_T(\Delta 2\theta) = \begin{cases} (1/\gamma_T)\exp(\Delta 2\theta/\gamma_T) & \text{for } \Delta 2\theta < 0 \\ 0 & \text{elsewhere} \end{cases} \quad (47)$$

where $\gamma_T \equiv \sin 2\theta/2\mu R$ for the linear absorption coefficient μ and the goniometer radius R. The angular dependence of the profile is shown in Fig. 5(*a*).

By applying the scale transform defined as

$$\gamma_3(2\theta) = (\sin 2\theta)/2 \quad (48)$$

and

$$G_3(2\theta) = -\ln[(1+\cos 2\theta)/(1-\cos 2\theta)], \quad (49)$$

the instrumental function independent of 2θ is given by

$$w_T(x) = \begin{cases} (1/\beta_T)\exp(x/\beta_T) & \text{for } x < 0 \\ 0 & \text{elsewhere} \end{cases} \quad (50)$$

with

$$\beta_T = (\mu R)^{-1}. \quad (51)$$

The profile on the transformed scale is shown in Fig. 5(*b*).

The Fourier transform of $w_T(x)$ is given by

$$W_T(\xi) \equiv \int_{-\infty}^{\infty} w_T(x)\exp(2\pi i\xi x)\,dx = (1 - 2\pi i\xi\beta_T)/(1 + 4\pi^2\xi^2\beta_T^2). \quad (52)$$

3.4. Spectroscopic profile of Cu *Kα* radiation

The effect of the spectroscopic profile of the Cu $K\alpha$ source is approximated by the sum of two Lorentzian functions as follows:

$$p_X(2\theta) = (1-\rho)f_L(2\theta; 2\theta_1, w_1) + \rho f_L(2\theta; 2\theta_2, w_2), \quad (53)$$

$$f_L(x; x_i, w_i) = (1/\pi w_i)\{1 + [(x - x_i)/w_i]^2\}^{-1}, \quad (54)$$

$$2\theta_2 = 2\arcsin[\lambda_2 \sin(2\theta_1/2)/\lambda_1], \quad (55)$$

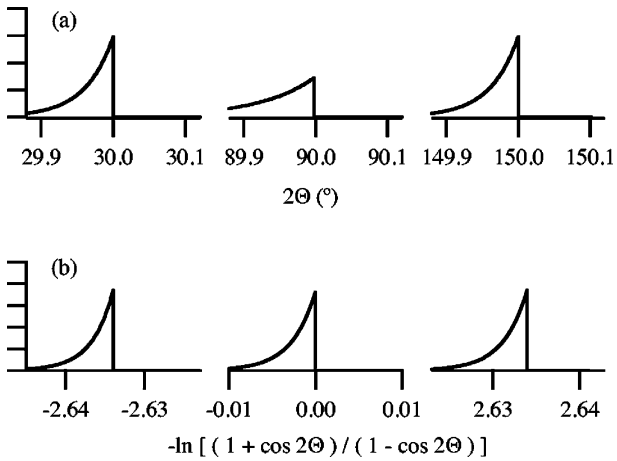

Figure 5
The dependence of the sample-transparency aberration function on the diffraction angle. (*a*) The instrumental function $\omega_T(\Delta 2\theta)$ on the 2θ scale, for the penetration depth of $\mu^{-1} = 0.5$ mm and the goniometer radius of R = 185 mm, and (*b*) that plotted on the $-\ln[(1+\cos 2\theta)/(1-\cos 2\theta)]$ scale.

$$w_i = \Delta\lambda_i \tan\theta_i, \quad (56)$$

where ρ is the fraction of the $K\alpha_2$ intensity, and λ_i and $\Delta\lambda_i$ are the wavelength and the full width at half-maximum, respectively, of the $K\alpha_i$ peak. Although many reports on the experimental estimation of the spectroscopic profile of Cu $K\alpha$ radiation are available (Compton & Allison, 1935; Bearden & Shaw, 1935; Hölzer *et al.*, 1997), the effective spectroscopic parameters for a diffractometer may be different if a crystal monochromator and/or pulse height analyser is used (Gangulee, 1970). For example, the parameters are approximately given as $\rho = 1/3$, $\lambda_1 = 1.5405981$ Å (Deslattes & Henins, 1973), $\lambda_2 = 1.54443$ Å, $\Delta\lambda_1 = 0.00058$ Å, $\Delta\lambda_2 = 0.00077$ Å (Compton & Allison, 1935).

For the purpose of elimination of the $K\alpha_2$ peak, the instrumental function

$$\omega_{X2}(\Delta 2\theta) = (1-\rho)\delta(\Delta 2\theta) + \rho f_L(\Delta 2\theta; 2\theta_2 - 2\theta_1, w_2 - w_1), \quad (57)$$

where $\delta(x)$ is the Dirac delta function, is used for the deconvolution. The total spectroscopic profile function is given by the convolution of the single $K\alpha_1$ profile with $\omega_{X2}(\Delta 2\theta)$ as

$$p_X(2\theta) = f_L(2\theta; 2\theta_1, w_1) * \omega_{X2}(2\theta). \quad (58)$$

Following Bragg's law $\lambda = 2d\sin\theta$,

$$\Delta\lambda/\Delta 2\theta = d\cos\theta, \quad (59)$$

which gives

$$\Delta\lambda/\lambda = 1/2\tan\theta. \quad (60)$$

Therefore, the scale transform required for the elimination of the $K\alpha_2$ peak is $G_2(2\theta) = \ln(\sin\theta)$, similarly to the higher-angle component of the axial divergence aberration function.

Fig. 6 briefly illustrates the effect of the scale transform on the spectroscopic profile function.

The instrumental function independent of the diffraction angle is given by

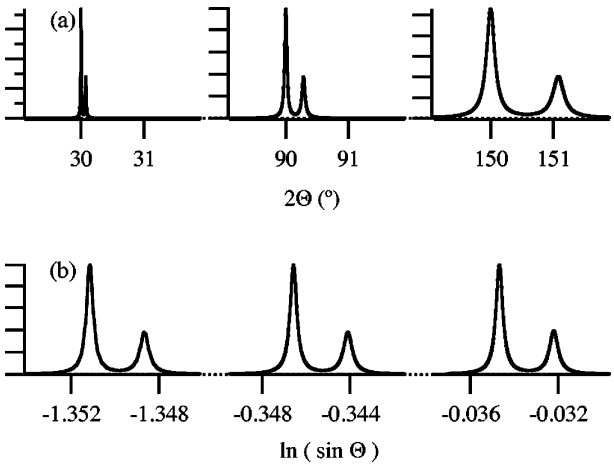

Figure 6
The dependence of the Cu $K\alpha$ spectroscopic profile on the diffraction angle. (*a*) The spectroscopic function $p_X(2\theta)$ on the 2θ scale, and (*b*) that plotted on the $\ln(\sin\theta)$ scale.

$$w_{X2}(x) = (1 - \rho)\delta(x) + \rho f_L(x; x_2, \gamma_2), \quad (61)$$

with

$$x_2 = (\lambda_2 - \lambda_1)/\lambda_1 \quad (62)$$

and

$$\gamma_2 = (\Delta\lambda_2 - \Delta\lambda_1)/2\lambda_1, \quad (63)$$

the analytical Fourier transform of which is given by

$$W_{X2}(\xi) = 1 - \rho + \rho \exp(-2\pi\xi\gamma_2)[\cos(2\pi\xi x_2) + i \sin(2\pi\xi x_2)]. \quad (64)$$

3.5. The effects of the geometry of the beam source and the receiving slit

An X-ray source with line focus is used for the Bragg–Brentano diffractometer and the receiving slit is located at the other focal position. Since the beam source has finite width along the equatorial direction, it can slightly broaden the line width according to the spatial intensity distribution of the radiation. The effects of the finite width of the beam source and the receiving slit are both represented by instrumental functions independent of the diffraction angle.

The instrumental function for the finite width of the receiving slit is given by the following form with a rectangular shape:

$$w_{RS}(x) = \begin{cases} 1/\gamma_{\rm RS} & \text{for } -\gamma_{\rm RS}/2 < x < \gamma_{\rm RS}/2 \\ 0 & \text{elsewhere} \end{cases} \quad (65)$$

with

$$\gamma_{\rm RS} = \arctan(W_{\rm RS}/R), \quad (66)$$

where $W_{\rm RS}$ is the width of the receiving slit and R is the goniometer radius. The Fourier transform of this function is given by

$$W_{RS}(\xi) = [\exp(\pi i \xi \gamma_{RS}) - 1]/\pi i \xi \gamma_{RS}. \quad (67)$$

The fundamental resolution of the diffractometer is usually dominated by the ratio $W_{\rm RS}/R$, because the width of the receiving slit is larger than the effective width of the beam source. Practically, the fundamental resolution can be modeled by the Gaussian function

$$w_R(x) = (1/\pi^{1/2}\gamma_R) \exp[-(x/\gamma_R)^2], \quad (68)$$

with the FWHM of $2(\ln 2)^{1/2}\gamma_R$, which can be approximated by $\gamma_{\rm RS}$ given in equation (66).

4. Analysis of experimental data

In this section, the $K\alpha_2$ lines and the aberrations caused by the axial divergence, flat specimen and sample transparency are removed from the whole experimental diffraction pattern of Si standard powder by the deconvolution technique. As a result of the deconvolution, the peak profiles in the lower-angle region will be dominated by the fundamental resolution or the receiving slit width, while those in the higher-angle region will be dominated by the spectroscopic profile of the $K\alpha_1$ radiation. Although it is not difficult to deconvolute the effects of the receiving slit and $K\alpha_1$ profile, they are left as a convolution in the current analysis, because the deconvolution of the above effects would result in very narrow deconvoluted profiles for the well crystallized Si sample, where severe loss of information may be caused by the finite interval of the data sampling.

4.1. Experimental

The standard Si powder (NIST SRM640*b*) was loaded into a hollow, of depth 0.549 (7) mm, of a glass holder with the filling factor of 46.8 (6)%. The penetration depth of the Cu $K\alpha$ X-ray was estimated at 0.140 (2) mm, which is sufficiently shorter than the thickness of the sample.

The powder diffraction pattern was measured with a conventional powder X-ray diffractometer (Rigaku RAD2C) with a Cu $K\alpha$ radiation tube operated as a line focus at 40 kV and 30 mA and a curved graphite monochromator on the diffracted-beam side. The radius of the goniometer circle was R = 250 mm; a receiving sit of 0.15 mm width and 1° open divergence, and scattering slits were used. The axial divergence was limited to Φ_A = 2.5° by the symmetrically located sets of Soller slits. The pattern was scanned over the angular range 20–155° (2θ), with a step length of 0.02° (2θ) and a counting time of 10 s step^{-1}.

4.2. Calculation

All calculations were conducted with commercial software for data analysis (*WaveMetrics*, *IgorPro*) on a personal computer (Apple, iBook, PowerPC G3 500 MHz). The built-in cubic spline and fast Fourier transform functions were utilized.

The data were deconvoluted by the following three steps.

(i) The elimination of $K\alpha_2$ and the higher-angle component of the axial divergence aberration on the $\ln(\sin\theta)$ scale.

(ii) The elimination of the lower-angle component of the axial divergence aberration and flat-specimen aberration on the $-\ln(\cos\theta)$ scale.

(iii) The elimination of the aberration caused by the sample transparency on the $-\ln[(1 + \cos 2\theta)/(1 - \cos 2\theta)]$ scale.

The total number of source data points was 6751, while a larger number of interpolated data were temporarily created for each deconvolution process; 65 536, 65 536 and 16 384 data, including 190-, 216- and 13-point zero-padding, were created for the first, second and third steps, respectively.

On the elimination of the $K\alpha_2$ peak, the following parameters were assumed: the intensity ratio, ρ = 1/3; the difference of the wavelength between $K\alpha_2$ and $K\alpha_1$, $(\lambda_2 - \lambda_1)/\lambda_1$ = 0.002480; the slight broadening of the $K\alpha_2$ peak, $(\Delta\lambda_2 - \Delta\lambda_1)/2\lambda_1$ = 0.00006.

The FWHM values of the Gaussian filter for noise suppression were 3.88×10^{-5} on the $\ln(\sin\theta)$ scale at the step (i), 4.16×10^{-5} on the $-\ln(\cos\theta)$ scale at step (ii), and 5.17×10^{-4} on the $-\ln[(1 + \cos 2\theta)/(1 - \cos 2\theta)]$ scale at step (iii). On the 2θ scale, the broadening in the Gaussian FWHM is given by

$$\Delta\Gamma_G^2 = \Gamma_1^2 \tan^2\theta + \Gamma_2^2/\tan^2\theta + \Gamma_3^2 \sin^2 2\theta, \quad (69)$$

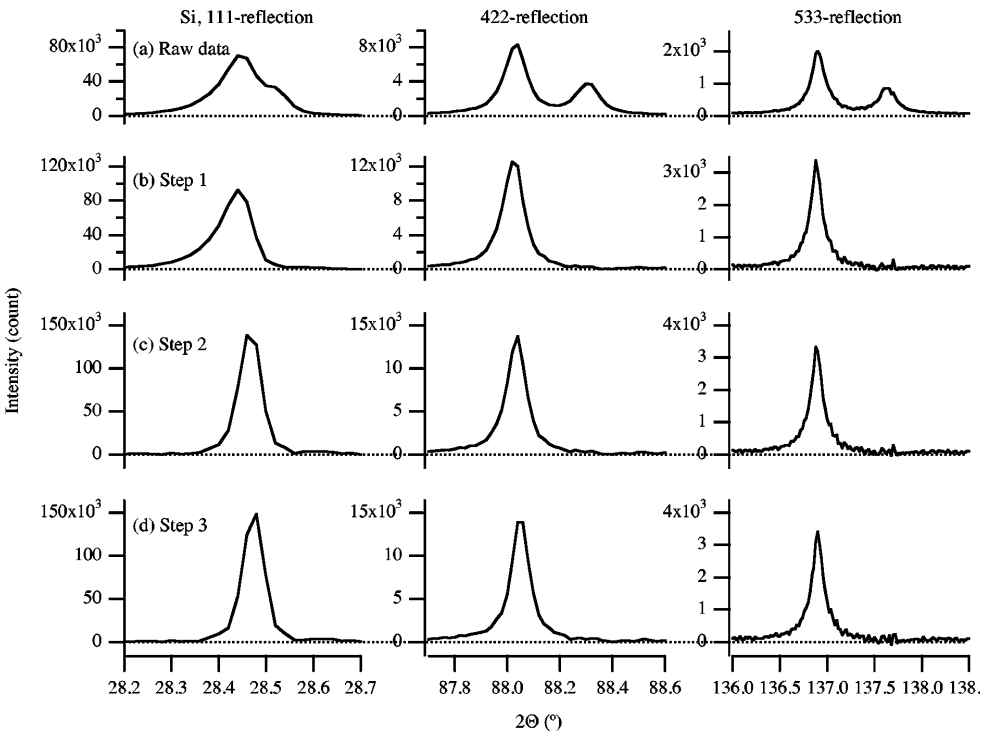

Figure 7
The changes in the diffraction profiles at each deconvolution step. (*a*) The raw data of the diffraction profiles of Si (NIST SRM640*b*), (*b*) the results of the deconvolution of $K\alpha_2$ and the higher-angle component of the axial divergence effect, (*c*) the results of the deconvolution of the lower-angle component of the axial divergence effect and the flat-specimen effect, and (*d*) the results of the deconvolution of the sample-transparency effect.

with

$$\Gamma_1 = 0.00444^\circ, \quad \Gamma_2 = 0.00476^\circ, \quad \Gamma_3 = 0.01481^\circ,$$

for each value of 2θ.

The fast Fourier algorithm enables rapid calculation for processing the large number of data. The deconvolution and the evaluation of the errors have been completed in 20 s by a program written in the macro language *IgorPro*.

4.3. Results of deconvolution

Fig. 7 shows how the peak profiles of 111, 422, 533 reflections are modified by each step of the deconvolution.

At the first step (Fig. 7*b*), where $K\alpha_2$ and the higher-angle part of the axial divergence effect are deconvoluted, it is found that not only the $K\alpha_2$ peaks for all reflections, but also the higher-angle tail of the 533 reflection is significantly removed by the deconvolution. At the second step (Fig. 7*c*), where the lower-angle part of the axial divergence effect and the flat-specimen effect are deconvoluted, the lower-angle tail of the 111 reflection is removed, and also the peak shift is automatically corrected. The effect of the third step (Fig. 7*d*), where the sample transparency effect is deconvoluted, is not very significant, but it seems that the lower angle tail of the 422 reflection is reduced and the slight peak shift is corrected. As a result, all the peak profiles obtained by the deconvolution of the instrumental functions from the experimental Si powder diffraction pattern have become narrow and symmetrical single-peak profiles.

4.4. Peak profile analysis

The diffraction profile data obtained by the deconvolution are analysed by a profile fitting and compared with the results of fitting to the raw data. We also compare the least-squares results applying the two different indicators of error, the square root of the reciprocal of the diagonal elements of the weight matrix, $\{\delta_n\}$, and the square root of the diagonal elements of the covariance matrix, $\{\varepsilon_n\}$.

The raw data are fitted by applying the model function synthesized by the convolution of the pseudo-Voigt function (Thompson *et al.*, 1987) with the instrumental function (Ida & Kimura, 1999*b*), where the Gaussian FWHM is fixed at 0.003438°, which is the value calculated by equation (66). The deconvoluted profiles are simply fitted by the pseudo-Voigt function, where the Gaussian FWHM is corrected by equation (69). In both of the fitting analyses, the location of the $K\alpha_1$ peak $2\theta_1$, the integrated intensity I, the Lorentzian width Γ_L, and the constant background b are treated as variable fitting parameters. Even though the convoluted model profile function is evaluated by an efficient algorithm (Ida & Kimura, 1999*b*), the fitting of the pseudo-Voigt function to the deconvoluted data is much more rapid in computation and easier to implement.

The results of the fitting are shown in Figs. 8, 9 and 10 for the 111, 422 and 533 peaks, respectively. The deconvoluted peak profiles are very well fitted by the symmetric pseudo-Voigt function. The fitting curves optimized for the two different indicators of error are almost identical. The difference between the deconvoluted data and the fitting curve lies roughly within $\{\delta_n\}$, and no significant systematic deviation is found. The indicator denoted by $\{\varepsilon_n\}$ tends to overestimate the errors in the deconvoluted data, as is clearly seen in the difference plots for the 422 and 533 reflections.

The profile parameters optimized by the fitting method are listed in Tables 1–3. The values obtained by the profile fitting to the deconvoluted data are close to those obtained by the direct analysis of the raw data. The slight difference can be caused by the assumed spectroscopic parameters of the source X-ray, which are not optimized for the current diffractometer.

The standard errors of the fitting parameters, which are the square root of the diagonal elements of the covariance matrix

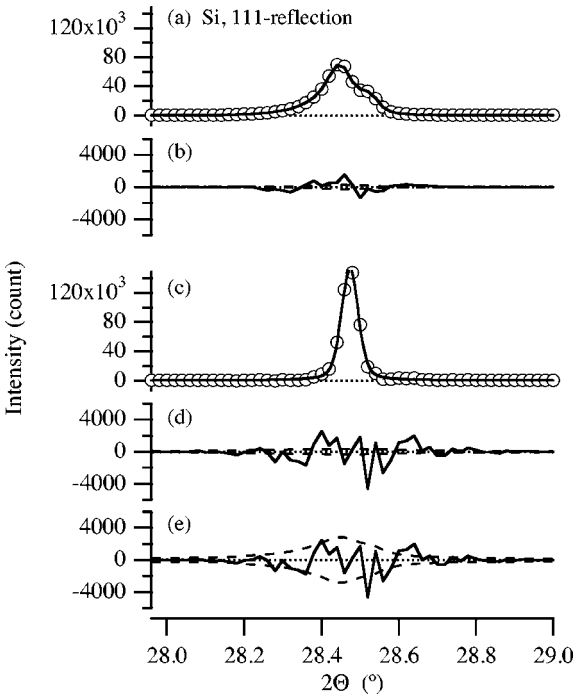

Figure 8
The results of profile fitting to the Si 111 reflection. (*a*) The raw data (open circles) and the fitting curve (solid line), (*b*) the difference plot (solid line) of the fitting to the raw data and the standard deviation (broken lines), (*c*) the deconvoluted data (open circles) and the fitting curve (solid line) optimized for the weight $\{\delta_n^{-2}\}$, (*d*) the error indicator $\{\delta_n\}$ (broken lines) and the difference (solid line) in the $\{\delta_n^{-2}\}$-weight fitting, and (*e*) the error indicator $\{\varepsilon_n\}$ (broken lines) and the difference (solid line) in the $\{\varepsilon_n^{-2}\}$-weight fitting.

for the parameters, are shown in parentheses in the tables. In the case of $\{\varepsilon_n^{-2}\}$-weight fitting to the deconvoluted data, the estimated error values are several to ten times larger than those estimated by the fitting to the raw data, which corresponds to the overestimation of the error in the indicator $\{\varepsilon_n\}$. The errors estimated by the $\{\delta_n^{-2}\}$-weight fitting are similar to or at most three times larger than those estimated from the fitting to the raw data. Therefore, it is concluded that the square root of the reciprocal diagonal elements of the weight matrix (*i.e.* the inverse matrix of the covariance matrix), $\{\delta_n\}$, is more appropriate than the square root of the diagonal elements of the covariance matrix, $\{\varepsilon_n\}$, as the indicator of the error in the deconvoluted data.

Tables 1–3 also list the R factors for profile fitting, $R_{\rm wp}$ and R_p, defined by

$$R_{\rm wp} \equiv \left\{ \frac{\sum_i w_i [Y(2\theta_i)_{\rm obs} - Y(2\theta_i)_{\rm calc}]^2}{\sum_i w_i Y(2\theta_i)_{\rm obs}^2} \right\}^{1/2}, \qquad (70)$$

and

$$R_p \equiv \frac{\sum_i |Y(2\theta_i)_{\rm obs} - Y(2\theta_i)_{\rm calc}|}{\sum_i Y(2\theta_i)_{\rm obs}}, \qquad (71)$$

where $Y(2\theta_i)_{\rm obs}$ is the observed profile intensity, $Y(2\theta_i)_{\rm calc}$ the calculated intensity, and w_i the weight for each datum. The values listed in Tables 1–3 clearly show larger values of the R factors for the fitting to the deconvoluted data. However, it seems that this is not a serious problem for the purpose of evaluating the profile parameters. Lower resolution and/or

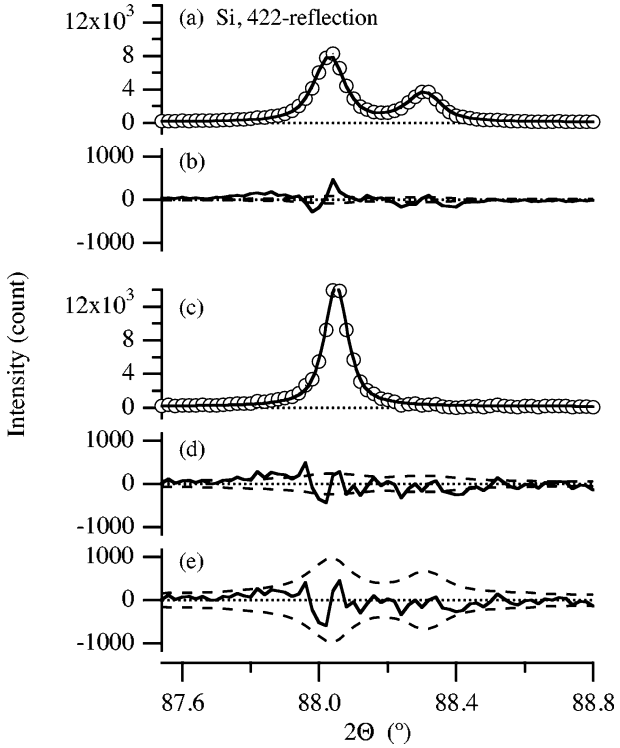

Figure 9
The results of profile fitting to the Si 422 reflection. See Fig. 8 for definitions.

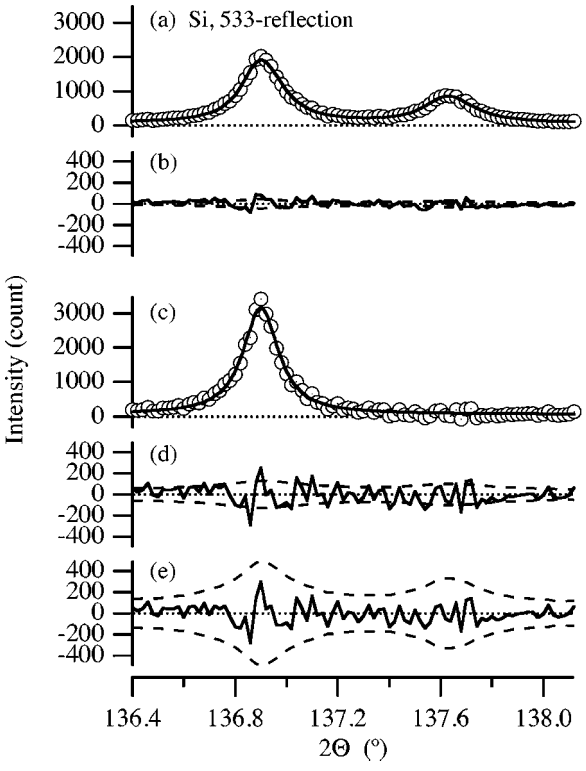

Figure 10
The results of profile fitting to the Si 533 reflection. See Fig. 8 for definitions.

Table 1
Profile parameters for Si 111 reflection.

$2\theta_1$ is the position of the $K\alpha_1$ peak, I is the integrated intensity, Γ_L is the FWHM of the Lorentzian broadening, and b is the constant background.

		Deconvoluted data	
	Raw data	$\{\delta_n^{-2}\}$	$\{\varepsilon_n^{-2}\}$
$2\theta_1$ (°)	28.47323 (9)	28.47354 (5)	28.4735 (4)
I	10280 (15)	9847 (23)	10313 (168)
Γ_L (°)	0.0098 (2)	0.0069 (2)	0.009 (2)
b	89 (5)	92 (17)	65 (45)
R_{wp} (%)	3.2	4.4	8.9
R_p (%)	2.2	6.9	6.8

Table 2
Profile parameters for Si 422 reflection.

See Table 1 for definitions.

		Deconvoluted data	
	Raw data	$\{\delta_n^{-2}\}$	$\{\varepsilon_n^{-2}\}$
$2\theta_1$ (°)	88.0481 (3)	88.0496 (6)	88.049 (2)
I	1742 (8)	1712 (21)	1733 (67)
Γ_L (°)	0.0271 (7)	0.023 (2)	0.024 (5)
b	92 (3)	116 (12)	113 (30)
R_{wp} (%)	8.1	8.4	11.3
R_p (%)	5.5	8.7	9.1

Table 3
Profile parameters for Si 533 reflection.

See Table 1 for definitions.

		Deconvoluted data	
	Raw data	$\{\delta_n^{-2}\}$	$\{\varepsilon_n^{-2}\}$
$2\theta_1$ (°)	136.8993 (8)	136.900 (2)	136.899 (6)
I	786 (8)	797 (18)	807 (53)
Γ_L (°)	0.050 (3)	0.049 (6)	0.05 (2)
b	67 (4)	57 (10)	54 (25)
R_{wp} (%)	6.4	12.4	14.9
R_p (%)	5.2	13.7	14.0

higher background in data tend to give smaller R factors despite the clear degradation in the informational quality. It is suggested that R factors for profile fitting are not always good indicators of either the quality of the source data or the validity of the theoretical models.

5. Conclusions

The effects of dominant aberrations in powder diffractometers with conventional geometry are effectively deconvoluted from the experimental diffraction patterns, by utilizing a fast Fourier method accompanied by scale-transform and interpolation of data. The errors in the deconvoluted data are approximated by the square root of the reciprocal diagonal elements of the weight matrix, which are estimated as the correlation of the reciprocal variance of the source data with the squared instrumental function. As the peak profiles in the deconvoluted data are modelled by symmetrical functions for well crystallized samples, the data analysis based on least-squares fitting becomes much faster in terms of computation time and easier to implement. It is also expected that the effects of finite size, dislocations and stacking faults in the crystallites are sensitively detected, because the intrinsic peak profiles caused by crystallographic imperfection can be reasonably extracted by the deconvolution method.

APPENDIX *A*

A1. Covariance matrix after deconvolution

The deconvolution of the instrumental function is equivalent to the convolution of the 'inverse instrumental function'. When the source data, deconvoluted data and inverse instrumental function are expressed by $\{y_n\}$, $\{z_n\}$ and $\{w_n^{(-1)}\}$, respectively, this relation is given by

$$z_n = \sum_{m=0}^{N-1} y_m w_{n-m}^{(-1)}. \tag{72}$$

The average of z_n, $\langle z_n \rangle$, is related to the average of y_n by

$$\langle z_n \rangle = \left\langle \sum_{m=0}^{N-1} y_m w_{n-m}^{(-1)} \right\rangle = \sum_{m=0}^{N-1} \langle y_m \rangle w_{n-m}^{(-1)}. \tag{73}$$

Therefore, the covariance matrix (S_{mn}) of the deconvoluted data is given by

$$\begin{aligned} S_{mn} &= \big\langle (z_m - \langle z_m \rangle)(z_n - \langle z_n \rangle) \big\rangle \\ &= \left\langle \sum_{k=0}^{N-1} (y_k - \langle y_k \rangle) w_{m-k}^{(-1)} \sum_{l=0}^{N-1} (y_l - \langle y_l \rangle) w_{n-l}^{(-1)} \right\rangle \\ &= \sum_{k=0}^{N-1} \sum_{l=0}^{N-1} \big\langle (y_k - \langle y_k \rangle)(y_l - \langle y_l \rangle) \big\rangle w_{m-k}^{(-1)} w_{n-l}^{(-1)}. \end{aligned} \tag{74}$$

When the covariance matrix of the source data is diagonal and the diagonal element is given by $\{\sigma_n^2\}$,

$$\big\langle (y_k - \langle y_k \rangle)(y_l - \langle y_l \rangle) \big\rangle = \begin{cases} \sigma_k^2 & \text{for} \quad k = l \\ 0 & \text{for} \quad k \neq l \end{cases} \tag{75}$$

Equations (74) and (75) give the matrix elements of the covariance matrix of the deconvoluted data as

$$S_{mn} = \sum_{k=0}^{N-1} \sigma_k^2 w_{m-k}^{(-1)} w_{n-k}^{(-1)}. \tag{76}$$

A2. Least-squares fitting to the deconvoluted data

The weighted least-squares fitting is identical to the problem of minimizing the following quantity:

$$\chi^2 = \sum_{k=0}^{N-1} \sigma_k^{-2} [y_k - g(x_k)]^2, \tag{77}$$

where $\{\sigma_n^2\}$ is the variance and $g(x)$ is the model function. When the data $\{y_n\}$ are the convolution of $\{z_n\}$ and the instrumental function $\{w_n\}$, and the model $g(x)$ is also the convolution of a function $f(x)$ and $\{w_n\}$, they are related by the following equations:

$$y_k = \sum_{n=0}^{N-1} z_n w_{k-n} \tag{78}$$

and

$$g(x_k) = \sum_{n=0}^{N-1} f(x_n) w_{k-n}. \tag{79}$$

Therefore, the objective function for the weighted least-squares method is written as

$$\begin{aligned}\chi^2 &= \sum_{k=0}^{N-1} \sigma_k^{-2} \left\{ \sum_{n=0}^{N-1} [z_n - f(x_n)] w_{k-n} \right\}^2 \\ &= \sum_{k=0}^{N-1} \sigma_k^{-2} \sum_{m=0}^{N-1} \sum_{n=0}^{N-1} [z_m - f(x_m)][z_n - f(x_n)] w_{k-m} w_{k-n} \\ &= \sum_{m=0}^{N-1} \sum_{n=0}^{N-1} [z_m - f(x_m)] T_{mn} [z_n - f(x_n)], \end{aligned} \tag{80}$$

where T_{mn} is the weight matrix given by

$$T_{mn} = \sum_{k=0}^{N-1} \sigma_k^{-2} w_{k-m} w_{k-n}. \tag{81}$$

Let us calculate the matrix elements of the product (U_{mn}) of the weight matrix (T_{mn}) and the covariance matrix (S_{mn}). The matrix element of (U_{mn}) is given by

$$\begin{aligned} U_{mn} &= \sum_{j=0}^{N-1} S_{mj} T_{jn} \\ &= \sum_{j=0}^{N-1} \sum_{k=0}^{N-1} \sigma_k^2 w_{m-k}^{(-1)} w_{j-k}^{(-1)} \sum_{l=0}^{N-1} \sigma_l^{-2} w_{l-j} w_{l-n} \\ &= \sum_{k=0}^{N-1} \sum_{l=l}^{N-1} \sigma_k^2 \sigma_l^{-2} w_{m-k}^{(-1)} w_{l-n} \sum_{j=0}^{N-1} w_{j-k}^{(-1)} w_{l-j}. \end{aligned} \tag{82}$$

When we apply the following relation to equation (82),

$$\sum_{k=0}^{N-1} w_k w_{n-k}^{(-1)} = \begin{cases} 1 & \text{for} \quad n = 0 \\ 0 & \text{for} \quad n \neq 0 \end{cases} \tag{83}$$

which is immediately derived from the definition of $w_n^{(-1)}$, the following result,

$$U_{mn} = \begin{cases} 1 & \text{for} \quad m = n \\ 0 & \text{for} \quad m \neq n \end{cases} \tag{84}$$

is derived; that is, (U_{mn}) is the unit matrix and (T_{mn}) is the inverse matrix of (S_{mn}).

References

Cheary, R. W. & Coelho, A. (1992). *J. Appl. Cryst.* **25**, 109–121.
Cheary, R. W. & Coelho, A. (1998). *J. Appl. Cryst.* **31**, 851–861.
Compton, A. H. & Allison, S. K. (1935). *X-rays in Theory and Experiment*. New York: D. Van Nostrand.
Bearden, J. A. & Shaw, C. H. (1935). *Phys. Rev.* **48**, 18–30.
Deslattes, R. D. & Henins, A. (1973). *Phys. Rev. Lett.* **31**, 972–975.
Gangulee, A. (1970). *J. Appl. Cryst.* **3**, 272–277.
Hölzer, G., Fritsch, M., Deutsch, M., Härtwig, J. & Förster, E. (1997). *Phys. Rev. A*, **56**, 4554–4568.
Ida, T. (1998*a*). *Rev. Sci. Instrum.* **69**, 2268–2272.
Ida, T. (1998*b*). *Rev. Sci. Instrum.* **69**, 3837–3839.
Ida, T. & Kimura, K. (1999*a*). *J. Appl. Cryst.* **32**, 634–640.
Ida, T. & Kimura, K. (1999*b*). *J. Appl. Cryst.* **32**, 982–991.
Keating, D. T. (1959). *Rev. Sci. Instrum.* **30**, 725–727.
Ladell, J., Parrish, W. & Taylor, J. (1959). *Acta Cryst.* **12**, 561–567.
Ladell, J., Zagofsky, A. & Pearlman, S. (1975). *J. Appl. Cryst.* **8**, 499–506.
Lipson, H. & Langford, J. I. (1999). *International Tables for Crystallography*, Vol. C, edited by A. J. C. Wilson & E. Prince, pp. 590–592. Dordrecht: Kluwer Academic Publishers.
Press, W. H., Flannery, B. P., Teukolsky, S. A. & Vetterling, W. T. (1986). *Numerical Recipes*. Cambridge University Press.
Rachinger, W. A. (1948). *J. Sci. Instrum.* **25**, 254–255.
Stokes, A. R. (1948). *Proc. Phys. Soc.* **61**, 382–391.
Thompson, P., Cox, D. E. & Hastings, J. B. (1987). *J. Appl. Cryst.* **20**, 79–83.